Optimizing the ionization-energy offset for enhanced photovoltaic properties in bilayer organic solar cells

Yuan Liu,[1] Jingjing Zhao,[1] Sein Chung,[2] Yexiao Huang,[3] Zhenmin Zhao,[1] Jeonggye Lee,[2] Hyukgu Yun,[2] Xiaoge Huang,[1] Safakath Karuthedath,[3] Kilwon Cho,[2] and Zhipeng Kan[1,*]

[1] *Center on Nanoenergy Research, Institute of Science and Technology for Carbon Peak & Neutrality, School of Physical Science & Technology, Guangxi University, Nanning 530004, China*

[2] *Department of Chemical Engineering, Pohang University of Science and Technology, Pohang 37673, South Korea*

[3] *Institute of Materials Research, Tsinghua Shenzhen International Graduate School, Tsinghua University, Shenzhen 518055, China*

(Received 5 October 2024; revised 23 December 2024; accepted 5 February 2025; published 4 March 2025)

The ionization-energy (IE) offset significantly impacts exciton dissociation and charge transfer in organic solar cells (OSCs). However, the optimal IE offset for efficient hole transfer remains uncertain. Herein, we explored the effect of IE offset on exciton dissociation and charge transfer in bilayer OSCs using simulations and experiments, focusing on PM6 as the donor and BTP-based acceptors (eC9-0Cl, eC9-2Cl, and eC9-4Cl). Varying the number of chlorine substitutions in the acceptors' terminal groups results in IE offsets of 0.23, 0.30, and 0.47 eV for PM6/eC9-0Cl, PM6/eC9-2Cl, and PM6/eC9-4Cl, respectively. With the IE offset of 0.47 eV, a power conversion efficiency (PCE) of 17.7% was achieved, while a 0.3 eV offset still attained a modest 16.4%. Simulations reveal three key findings: the IE offset directly influences the maximum PCE a device potentially achieves; the PCE is affected by the mobility of charge carriers but not by their type; and lower bimolecular recombination rates correlate with higher PCE. We found a minimum IE offset of 0.3 eV, carrier mobility of $1 \times 10^{-8}\,m^2/V\,s$, and bimolecular recombination rate of $1 \times 10^{-13}\,cm^3/s$ to achieve a PCE of over 20%. Our results provide guidelines for designing novel materials for high-efficiency bilayer OSCs.

DOI: 10.1103/PhysRevApplied.23.034006

I. INTRODUCTION

Organic solar cells (OSCs) have gained broad research interest owing to their significant advantages, such as being lightweight, highly flexible, semitransparent, and capable of roll-to-roll manufacturing [1–6]. The power conversion efficiency (PCE) of single-junction OSCs comprising polymer donor and nonfullerene acceptor (NFA) has reached over 20% [7,8]. NFAs absorb more photons and across a greater range to produce more excitons compared to fullerene acceptors. This, in turn, potentially increases photogenerated current density if the generated excitons are converted into free charges. In OSCs with wide-band-gap donors and low-band-gap NFAs, the charge generation depends on the ionization-energy (IE) offset between the donor and acceptor rather than their electron-affinity (EA) offset [9]. This requires a trade-off between voltage and current density in OSCs. However, the precise IE offset needed for effective hole transfer remains debatable and depends on the material of the system, the IE measurement methods, and processing conditions [10–12].

The dependence of photovoltaic performance on the energy offsets was investigated in bulk-heterojunction OSCs. To this end, six different donor-acceptor pairs, with the highest occupied molecular orbital (HOMO) offsets ranging from −0.05 to 0.21 eV, were used to fabricate OSCs. The performance of these devices was systematically evaluated to determine the influence of varying energy offsets on their photovoltaic characteristics. The results show that exciton (electron-hole pair) separation occurs when the IE offset is positive [13]. Through the design a series of polymeric donor PBDB-T derivatives for blending with NFAs Y6, the IE offsets ranged from 0.22 eV to 0.59 eV were attained [14]. It was discovered that a smaller IE offset decreased the nonradiative voltage loss. Additionally, it significantly reduced the charge transfer state dissociation efficiency and decreased photocurrent generation. This observation was consistent with previous results [15,16]. Therefore, a positive IE offset of 0.3 to 0.5 eV is necessary to promote effective exciton dissociation and subsequent charge generation. However, most of these works were based on bulk-heterojunction OSCs, where the donor and acceptor were blended in a bulk volume. The bulk blend induces severe energy bending and

*Contact author: kanzhipeng@gxu.edu.cn

increases the energetic disorder, which is detrimental to exploring the relationship between IE offset and device properties [10,14,17–19]. In contrast, bilayer OSCs comprise pristine donor and acceptor layers, providing an ideal structure without the energy bending to investigate the impact of IE offset.

In this work, we explored the impact of the IE offset on charge generation and recombination arising from exciton dissociation at the donor-acceptor interface in bilayer OSCs. To this end, PM6 was selected as the donor and paired with a set of BTP-based acceptors with different numbers of chlorine atoms in the terminal group. As such, the IE offsets of 0.23, 0.30, and 0.47 eV for PM6/eC9-0Cl, PM6/eC9-2Cl, and PM6/eC9-4Cl were achieved, respectively. When the acceptor was selectively photoexcited, the exciton dissociation efficiency increased with the increase of IE offset, resulting in values of 87.53%, 90.04%, and 92.98% for eC9-0Cl, eC9-2Cl, and eC9-4Cl, respectively. This observation was also noticed in the device simulations. In addition, the increase of IE offset effectively suppresses the bimolecular charge recombination from 1.88×10^{-12} to 7.06×10^{-13} cm^3/s, leading to improved short-circuit current (J_{SC}) and fill factor (FF), with values increased from 18.64 mA/cm^2, 58.26% to 27.24 mA/cm^2, 74.82%, respectively. To further understand the effect of IE offset on the photovoltaic performance of the device, we investigated the role of carrier mobility and bimolecular recombination rate under different IE offsets through device simulation. The results reveal that a higher PCE is attainable with a larger IE offset and that minimizing bimolecular recombination while maximizing carrier mobility is crucial for achieving a high PCE. Our results suggest that an IE offset of 0.3 eV is a prerequisite for attaining efficient photon-to-electron conversions in OSCs comprising BTP-based acceptors, providing insightful guidelines for novel material design and fabrication of high-performance bilayer OSCs.

II. RESULTS AND DISCUSSION

Figures 1(a) and 1(b) show the chemical structures of eC9-0Cl, eC9-2Cl, eC9-4Cl, and PM6 (where each *X* in Fig. 1(a) denotes 0, 1, or 2 Cl atoms, respectively). The normalized ultraviolet-to-visible (UV-vis) absorption spectra of donor and acceptor materials show a broad spectral range from 400 nm to nearly 950 nm [Fig. 1(c)]. The non-normalized UV-vis spectra can be seen in Fig. S1 within the Supplemental Material [20]. With increasing numbers of chlorine atoms, the absorption edge of the NFAs is redshifted from 785 to 830 nm, with a narrower

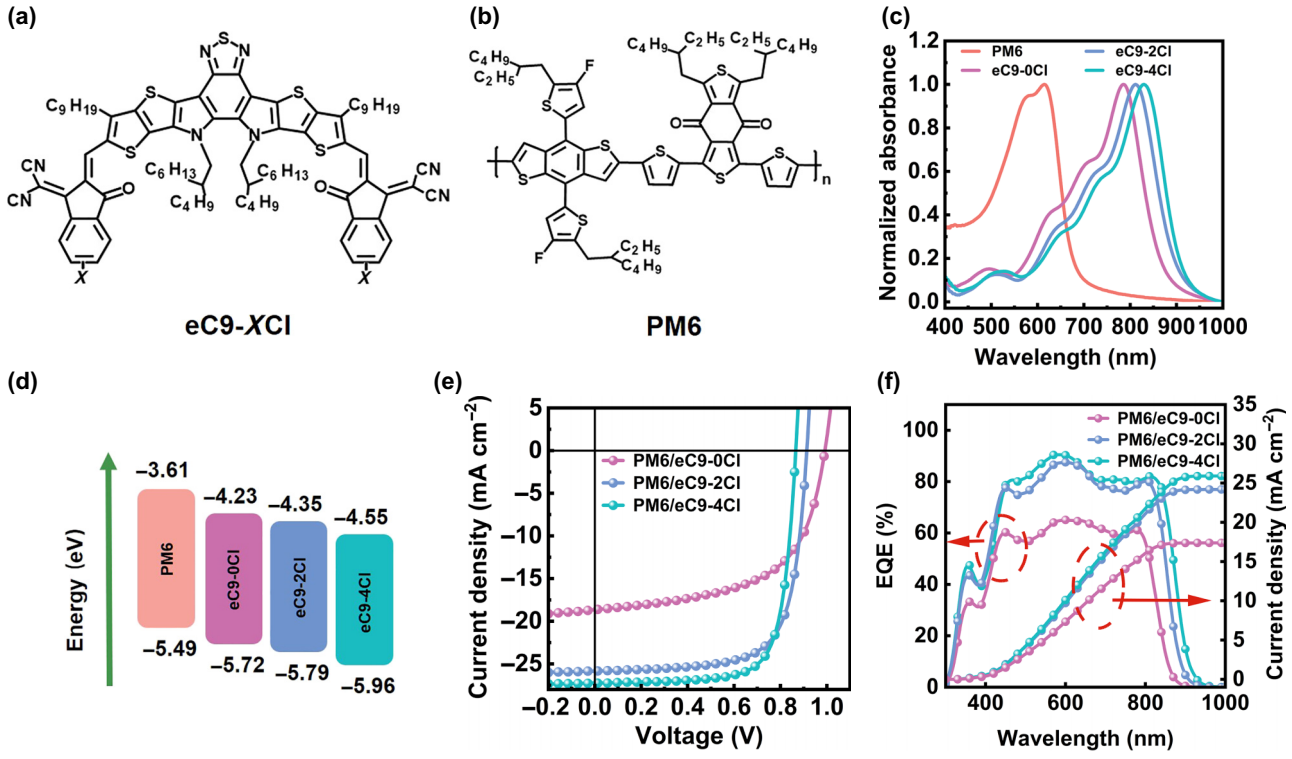

FIG. 1. (a),(b) Chemical structures of eC9-0Cl, eC9-2Cl, eC9-4Cl, and PM6; (c) normalized absorbance spectra of PM6, eC9-0Cl, eC9-2Cl, and eC9-4Cl neat films; (d) energy levels of PM6, eC9-0Cl, eC9-2Cl, and eC9-4Cl. (e) *J-V* characteristics of the bilayer organic solar cells (OSCs); (f) external quantum efficiency (EQE) spectra of the bilayer OSCs comprising PM6/eC9-0Cl, PM6/eC9-2Cl, and PM6/eC9-4Cl.

optical band gap and a larger IE offset. The IE values of the donors and acceptors in the thin films were determined by ultraviolet photoelectron spectroscopy, and the EA energies were estimated by adding the optical band gap of the materials (determined by the intersection of the normalized absorbance and photoluminescence spectra) to the IE. For detailed information on the analysis of IE and EA values see Fig. S2 and Table S1 within the Supplemental Material [21]. The introduction of chlorine atoms leads to gradual downshifts of the energy levels and decreased band gap. As presented in Fig. 1(d), the IE (EA) of PM6, eC9-0Cl, eC9-2Cl, and eC9-4Cl are −5.49 eV (−3.61 eV), −5.72 eV (−4.23 eV), −5.79 eV (−4.35 eV), and −5.96 eV (−4.55 eV), respectively, enabling a cascaded ΔIE ranging from 0.23 to 0.47 eV.

The *J-V* characteristics of the bilayer OSCs measured with AM1.5G simulated irradiance (100 mW/cm^2) are plotted in Fig. 1(e), and the detailed parameters are summarized in Table I. The fabrication of bilayer OSCs used the same protocol reported [6], and the solvent wash further confirmed the influence of the upper layer on the donor layer [see Fig. S7 within the Supplemental Material [22]]. The PM6/eC9-4Cl device exhibited a PCE of 17.67% with an open-circuit voltage V_{OC} of 0.867 V, a J_{SC} of 27.24 mA/cm^2, and an FF of 74.82%. The PM6/eC9-2Cl device resulted in a slightly lower PCE of 16.85% with a V_{OC} of 0.913 V, a J_{SC} of 25.83 mA/cm^2, and an FF of 71.43%. The PM6/eC9-0Cl device, on the other hand, managed to reach a modest PCE of only 10.78% with a V_{OC} of 0.992 V, a J_{SC} of 18.64 mA/cm^2, and a significantly reduced FF of 58.26%. The variation in V_{OC} of these devices is explained by the EA energy levels of eC9-4Cl and eC9-2Cl compared to eC9-0Cl. It is clear that with the increase of halogenated atoms, the nonfullerene band gap becomes narrower, and the EA energy level difference between the donor and acceptor becomes smaller. Comparing the eC9-4Cl system with high J_{SC} and high FF, the V_{OC} in the eC9-0Cl system obtained the maximum value of 0.992 V. However, the FF and J_{SC} of the device were indeed the lowest among the three systems, suggesting that the small IE offset hinders the charge generation and extraction [14]. The external quantum efficiency (EQE) spectra of these devices are shown in Fig. 1(f). The PM6/eC9-4Cl and PM6/eC9-2Cl-based devices exhibited a broader photon absorption range compared to the PM6/eC9-0Cl devices. This phenomenon originates from the redshifted absorption spectra of PM6/eC9-4Cl and PM6/eC9-2Cl, which possess a wider absorption range. In addition, the maximum EQE responses of PM6/eC9-0Cl, PM6/eC9-2Cl, and PM6/eC9-4Cl devices were 64.97%, 87.55%, and 90.49%, respectively, and the more significant EQE responses imply that the devices generate more photogenerated currents, which is consistent with J_{SC}. The integrated J_{SC} from EQE spectra were 17.38, 24.19, and 25.90 mA/cm^2 for PM6/eC9-0Cl, PM6/eC9-2Cl, and PM6/eC9-4Cl devices, respectively. The integrated J_{SC} obtained from EQE was consistent with the measured J_{SC} of devices under simulated solar light.

For the dark *J-V* characteristics of devices based on PM6/eC9-0Cl, PM6/eC9-2Cl, and PM6/eC9-4Cl, see Fig. S3 within the Supplemental Material [23]. It was observed that the devices based on PM6/eC9-2Cl and PM6/eC9-4Cl exhibited a lower leakage current compared to the PM6/eC9-0Cl device. Consequently, lower charge recombination and higher charge extraction processes are expected [24]. This observation corresponds with the higher FF exhibited by the PM6/eC9-2Cl and PM6/eC9-4Cl devices. To gain insights into the charge carrier dynamics, we carried out time-dependent measurements on the bilayer films and devices from the picosecond to microsecond range.

Figures 2(a)–2(c) show the time-resolved photoluminescence kinetics of neat NFAs and bilayer films with PM6. In neat acceptor films, light absorption results in the generation of excitons, and the obtained lifetime can be assigned as the singlet exciton lifetime. In bilayer films, excitons migrate towards the donor-acceptor interface, where they undergo separation into electrons and holes, driven by the energy provided by the IE offset—subsequently, the holes transfer from the NFA to PM6. The observed decrease in the lifetime of acceptor excitons in bilayer films compared to pure acceptor films indicates improved efficiency in exciton dissociation and enhanced hole transfer efficiency. We calculated the photoluminescence quenching efficiency (PLQE) and the corresponding hole transfer efficiency by using the equation $\tau_{av} = (\tau_1^2 + \tau_2^2)/(\tau_1 + \tau_2)$. The PLQE of PM6/eC9-0Cl, PM6/eC9-2Cl, and PM6/eC9-4Cl are 87.53%, 90.04%, and 92.98%, respectively, with PM6/eC9-4Cl demonstrating the optimal hole transfer

TABLE I. The photovoltaic parameters of the optimized OSCs were measured under AM1.5G (100 mW/cm^2) simulated irradiance. The values were averaged from ten independent devices. The J_{cal} value listed was the integral current of the EQE spectrum.

	V_{OC} (V)	J_{SC} (mA/cm^2)	J_{cal} (mA/cm^2)	FF (%)	PCE (%)
PM6/eC9-4Cl	0.867 (0.867 ± 0.002)	27.24 (26.83 ± 0.31)	25.90	74.82 (74.52 ± 0.53)	17.67 (17.33 ± 0.21)
PM6/eC9-2Cl	0.913 (0.913 ± 0.003)	25.83 (25.15 ± 0.48)	24.19	71.43 (71.19 ± 0.27)	16.85 (16.35 ± 0.33)
PM6/eC9-0Cl	0.992 (0.993 ± 0.003)	18.64 (18.34 ± 0.32)	17.38	58.26 (57.38 ± 0.58)	10.78 (10.45 ± 0.20)

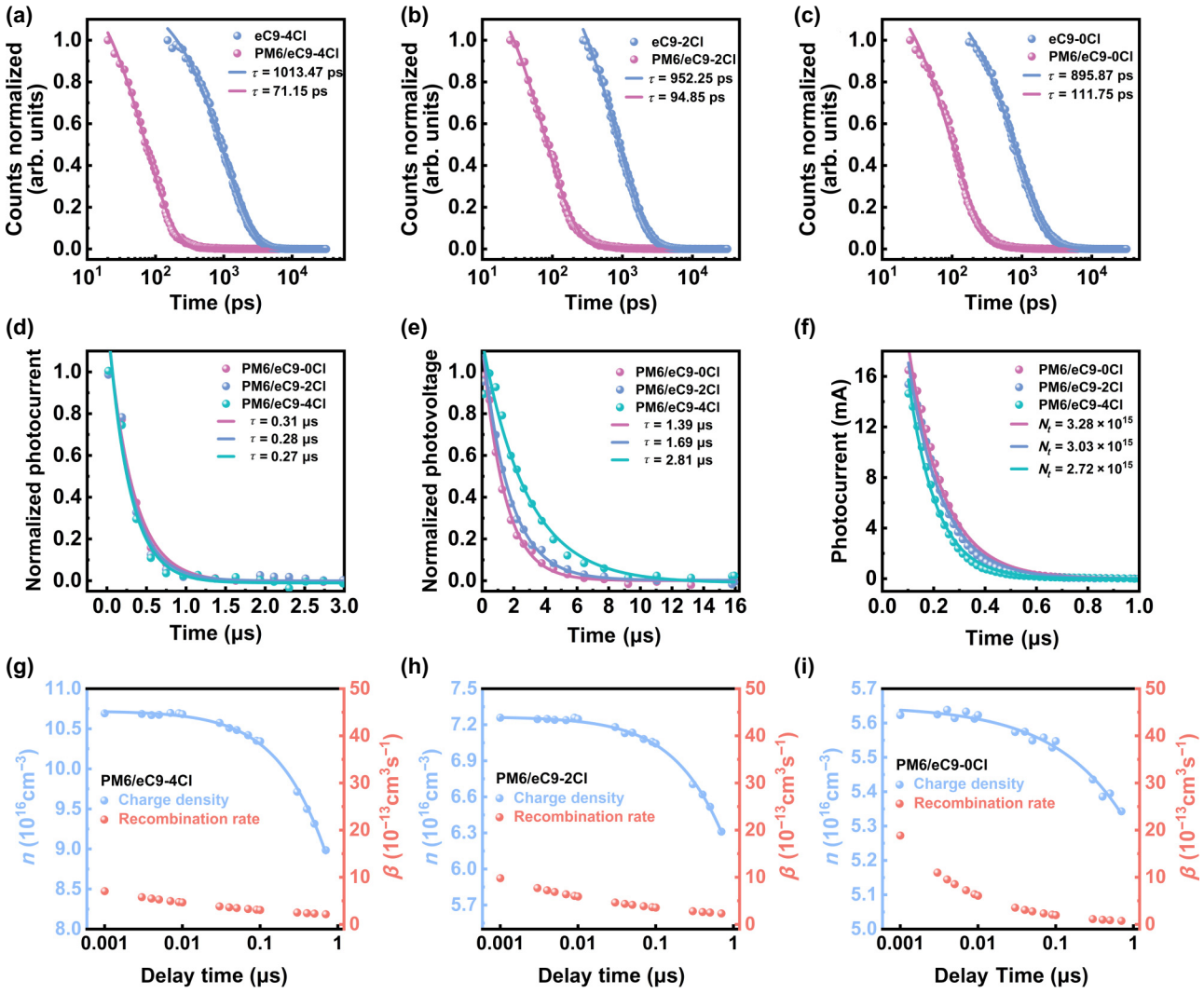

FIG. 2. Time-resolved photoluminescence spectra of (a) eC9-4Cl and PM6/eC9-4Cl films; (b) eC9-2Cl and PM6/eC9-2Cl films; and (c) eC9-0Cl and PM6/eC9-0Cl films. (d) Transient photocurrent; (e) transient photovoltage; and (f) deep-level transient spectroscopy fittings of the PM6/eC9-0Cl, PM6/eC9-2Cl, and PM6/eC9-4Cl devices. Charge carrier density as a function of the delay time of the (g) PM6/eC9-0Cl, (h) PM6/eC9-2Cl, and (i) PM6/eC9-4Cl devices.

efficiency of 92.98% [see Table S4 within the Supplemental Material [25]]. These findings suggest that the IE offset is a key factor limiting exciton dissociation and hole transport efficiency.

Then, we investigated the impact of IE offsets on charge carrier dynamics. Transient photocurrent and photovoltage measurements were used to attain information on charge carrier extraction and recombination during operation. Under short-circuit conditions, the PM6/eC9-0Cl, PM6/eC9-2Cl, and PM6/eC9-4Cl exhibit a photocurrent decay time of 0.31, 0.28, and 0.27 μs, respectively, as shown in Fig. 2(d). The extraction times of the devices PM6/eC9-2Cl and PM6/eC9-4Cl are superior to those of PM6/eC9-0Cl. The PM6/eC9-0Cl, PM6/eC9-2Cl, and PM6/eC9-4Cl have lifetimes τ of 1.39, 1.69, and 2.81 μs, respectively, which indicate that the nongeminate recombination of the PM6/eC9-4Cl device is the lowest [Fig. 2(e)]. Figure 2(f) shows the trap density obtained from deep-level transient spectroscopy [26,27]. The trap state density (N_t) of PM6/eC9-0Cl, PM6/eC9-2Cl, and PM6/eC9-4Cl were measured to be 3.23×10^{15} cm^{-3}, 3.03×10^{15} cm^{-3}, and 2.72×10^{15} cm^{-3}, respectively. This is consistent with previous reports that the higher the PCE, the lower the corresponding trap state density [28–31]. The lower density of trap states in the PM6/eC9-2Cl and PM6/eC9-4Cl devices compared to that of PM6/eC9-0Cl suggests that the PM6/eC9-2Cl and PM6/eC9-4Cl devices have lower trap recombination to generate higher photocurrents compared to PM6/eC9-0Cl [see Table S2 within the Supplemental Material [32]]. To characterize the rate of charge recombination during extraction, we used time-delayed photon-induced

charge carrier extraction with linearly increasing voltage to obtain information on charge extraction and recombination [33,34]. The carrier density as a function of the delay time is plotted in Figs. 2(g)–2(i) [see Table S3 within the Supplemental Material [35]]. Bimolecular recombination rates $\beta(t)$ ($t = 10$ ns) of PM6/eC9-0Cl, PM6/eC9-2Cl, and PM6/eC9-4Cl are 1.88×10^{-12}, 9.80×10^{-13}, and 7.06×10^{-13} cm^3/s, respectively. PM6/eC9-2Cl and PM6/eC9-4Cl have lower bimolecular recombination rates than PM6/eC9-0Cl. We note that the initially generated charge carrier densities were 5.65×10^{16}, 7.27×10^{16}, and 1.07×10^{17} cm^{-3} for PM6/eC9-0Cl, PM6/eC9-2Cl, and PM6/eC9-4Cl devices, respectively. These findings indicate that increasing the IE offset facilitates the dissociation of excitons, leading to a higher yield of photogenerated charges. The larger IE offset concurrently reduces bimolecular recombination and improves charge extraction, which in turn results in an enhancement of both the J_{SC} and FF. Detailed information is available [see Fig. S5 and Table S4 within the Supplemental Material [36]].

The impact of IE offset on the performance of the bilayer OSCs was also evident in the simulation results, offering insights into the device parameter correlations that are otherwise challenging to measure directly. For these simulations, the measured refractive indices, extinction coefficients, various IE offsets, and bimolecular recombination rates were used to model the *J-V* curves of OSCs under an incident light intensity of AM1.5G [Figs. 3(a)–3(c)]. The simulation software is commercial, namely SETFOS, which utilizes transfer matrix modeling to calculate charge generation within the active layer and numerically solves the drift-diffusion equation, thereby providing a comprehensive analysis of device performance. To differentiate from the bulk heterojunction, we used a device structure

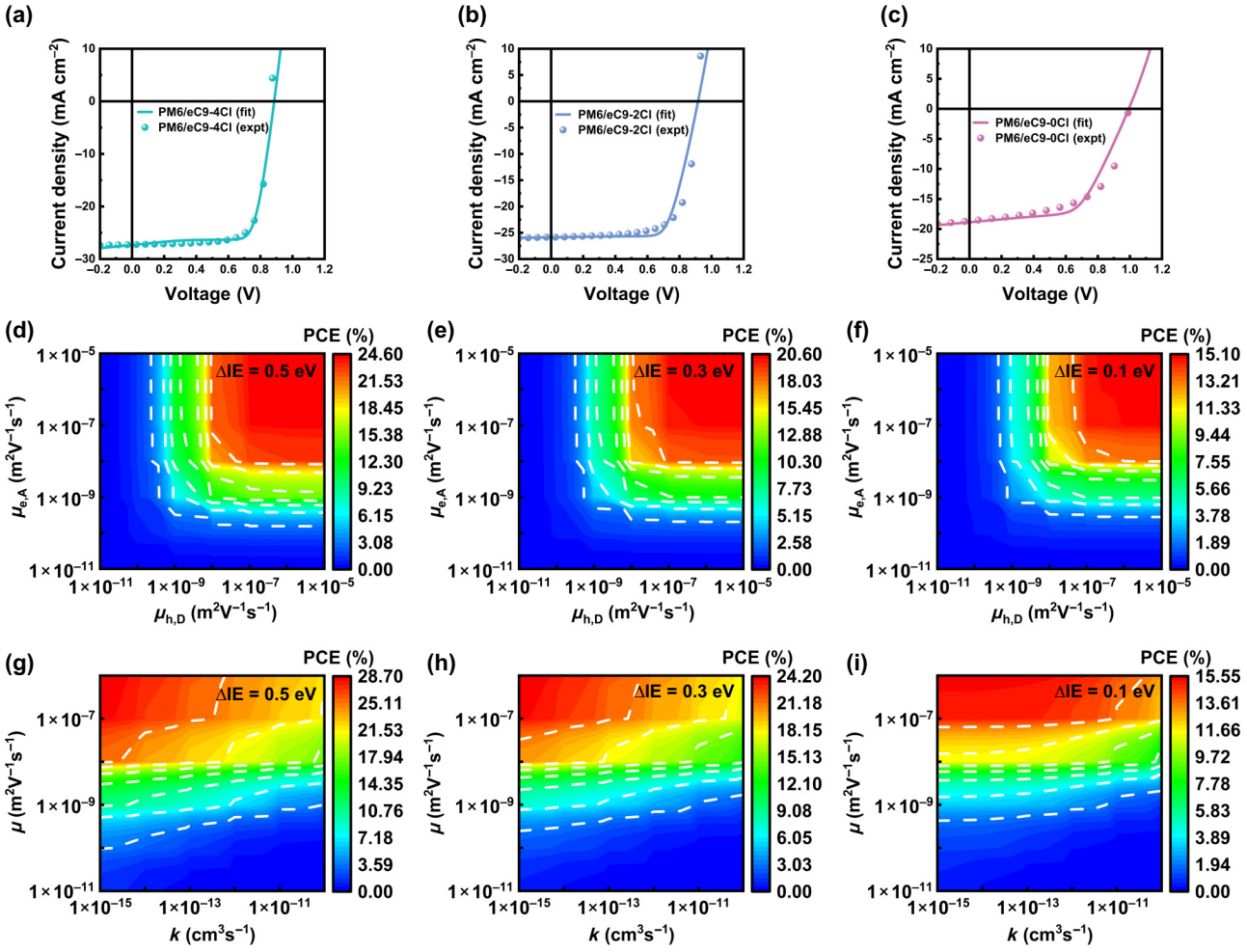

FIG. 3. *J-V* curves from simulation and experiment for (a) PM6/eC9-4Cl, (b) PM6/eC9-2Cl, and (c) PM6/eC9-0Cl. Effect of active layer carrier mobility μ on power conversion efficiency (PCE) at (d) $\Delta IE = 0.5$ eV; (e) $\Delta IE = 0.3$ eV; (f) $\Delta IE = 0.1$ eV. Effect of recombination rate β on PCE at (g) 0.5 eV; (h) 0.3 eV; (i) 0.1 eV (with an optical band gap of 1.88 eV for the donor and 1.64 eV, 1.44 eV, 1.24 eV, for the acceptor, respectively).

TABLE II. Simulated photovoltaic parameters of PM6/eC9-4Cl, PM6/eC9-2Cl, and PM6/eC9-0Cl devices.

	V_{OC} (V)	J_{SC} (mA/cm^2)	FF (%)	PCE (%)
PM6/eC9-4Cl	0.874	27.30	75.35	17.99
PM6/eC9-2Cl	0.915	25.86	71.89	17.01
PM6/eC9-0Cl	0.992	18.87	58.36	10.93

very close to the experimental device, adding an interfacial layer between the donor and acceptor layer [see Fig. S6 within the Supplemental Material [37]]. In the bilayer structure, holes are primarily considered the carriers in the donor layer, while electrons dominate in the acceptor layer. Therefore, the mobility of holes in the donor layer and electrons in the acceptor layer are critical factors. The effect of minority carrier mobility on the device performance can be neglected when the minority carrier mobility in the donor and acceptor layers is more than 3 orders of magnitude lower than that of the majority carrier mobility [see Fig. S10(c) within the Supplemental Material [38]]. The simulated photovoltaic parameters of the PM6/eC9-0Cl, PM6/eC9-2Cl, and PM6/eC9-4Cl devices are shown in Table II, and the remaining simulation parameters are listed in Table III. The J_{SC} of PM6/eC9-4Cl is 27.24 mA/cm^2, which is significantly higher than the 25.83 mA/cm^2 of PM6/eC9-2Cl and 18.64 mA/cm^2 of PM6/eC9-0Cl. In the preceding discussion, we believed that the difference in the J_{SC} was directly caused by the redshift of the absorption spectrum of PM6/eC9-4Cl, which is consistent with the wider response range of PM6/eC9-4Cl in the EQE, which is confirmed by the simulation results, where the effective density of states of PM6/eC9-4Cl (9.6×10^{-28} m^{-3}) is higher than that of PM6/eC9-2Cl (6.5×10^{-28} m^{-3}) and PM6/eC9-0Cl (2.3×10^{-28} m^{-3}). The simulated hole and electron mobilities for the PM6/eC9-4Cl device are 2.5×10^{-8} and 1×10^{-8} m^2/V s, respectively, which are higher than those for the PM6/eC9-2Cl (1.5×10^{-8} and 1×10^{-8} m^2/V s) and PM6/eC9-0Cl (8.2×10^{-9} and 7×10^{-9} m^2/V s) devices. Chlorination led to an increase in carrier mobility and thus an increase in PCE, which is consistent with previous reports [39,40]. Additionally, the trap density for the PM6/eC9-4Cl device is 1×10^{15} cm^{-3}, which is lower than that of the PM6/eC9-2Cl (8×10^{15} cm^{-3}) and PM6/eC9-0Cl (7×10^{16} cm^{-3}) devices. These findings are consistent with the observation that the PM6/eC9-4Cl device exhibits the highest values for both J_{SC} and FF. Therefore, the simulated result of the bilayer OSCs closely aligns with the experimental data, confirming the device simulator's validity and the simulation results' reliability.

Based on the experimental and simulated results, we believe that an IE offset of 0.3 eV is the minimum for the device to achieve high efficiency. Therefore, we chose the device PM6/eC9-2Cl as a case study to simulate the maximum PCE achievable with different IE offsets and further investigate the role of carrier dynamics with different IE offsets. In carrier dynamics, carrier mobility and bimolecular complexation are the key factors affecting OSCs efficiency. As shown in Figs. 3(d)–3(i), the optical band gap of the donor is 1.88 eV, the optical band gaps of the acceptor are 1.64, 1.44, and 1.24 eV, and the IE biases are 0.5, 0.3, and 0.1 eV, respectively. Figures 3(d)–3(f) show the effects of electron and hole mobility on PCE. When the electron (hole) mobility is lower than 1×10^{-8} m^2/V s, then a high PCE cannot be obtained no matter how high the hole (electron) mobility is, and the PCE does not increase with the mobility. At the same mobility, the higher the IE offset, the higher the PCE, which may be because a large IE offset favors the dissociation of excitons and thus the

TABLE III. Parameters of PM6/eC9-4Cl, PM6/eC9-2Cl, and PM6/eC9-0Cl devices via drift-diffusion simulations. LUMO is the lowest unoccupied molecular orbital, HOMO is the highest occupied molecular orbital, N_0 is the effective density of states, μ_e is the electron mobility, the μ_h is hole mobility, N_t is trap state density, β is the rate of bimolecular recombination, W_R is the anode work function, W_L is the cathode work function, E_t is the depth of the trap, ε_r is the relative dielectric constant, W_R, W_L, E_t, and ε_r are consistent in the device PM6/eC9-4Cl, PM6/eC9-2Cl, and PM6/eC9-0Cl.

	PM6/eC9-4Cl		PM6/eC9-2Cl		PM6/eC9-0Cl	
	Donor	Acceptor	Donor	Acceptor	Donor	Acceptor
LUMO (eV)	−3.61	−4.55	−3.61	−4.35	−3.61	−4.23
HOMO (eV)	−5.49	−5.96	−5.49	−5.79	−5.49	−5.72
N_0 (m^{-3})	9.6×10^{28}	9.6×10^{28}	6.5×10^{28}	6.5×10^{28}	2.3×10^{28}	2.3×10^{28}
μ_e (m^2/Vs)	1×10^{-11}	1×10^{-8}	1×10^{-11}	1×10^{-8}	6×10^{-10}	8.2×10^{-9}
μ_h (m^2/Vs)	2.5×10^{-8}	1×10^{-11}	1.5×10^{-8}	1×10^{-11}	8.2×10^{-9}	6×10^{-10}
N_t (cm^{-3})	1×10^{15}	1×10^{15}	8×10^{15}	8×10^{15}	7×10^{16}	7×10^{16}
β (cm^3 s^{-1})	7.06×10^{-13}	7.06×10^{-13}	9.80×10^{-13}	9.80×10^{-13}	1.89×10^{-12}	1.89×10^{-12}
W_R (eV)			5.20			
W_L (eV)			3.94			
E_t (eV)			0.3			
ε_r			3.5			

production of more carriers, which is consistent with the previous analysis.

In addition to carrier mobility, bimolecular complexation is known to affect the performance of OPVs significantly. Therefore, it is crucial to understand the effects of carrier mobility and bimolecular complexation on OPV performance. For the sake of this study, here we assume that the hole and electron mobilities are balanced ($\mu_h = \mu_e$). As shown in Figs. 3(g)–3(i), the higher the carrier mobility and the smaller the bimolecular complex, the higher the PCE the device can achieve, while the higher the IE offset, the higher the PCE. This can be attributed to the wider acceptor band gap absorption redshift, which can absorb more photons to generate a photogenerated charge, and it has been demonstrated that a larger IE offset facilitates hole transfer, thus generating enough current to offset the effect of V_{OC} drop and achieve a higher PCE. In conclusion, three key observations are made: first, a larger IE offset leads to a higher achievable PCE, with a maximum of 28.7% in single-junction bilayer OSCs; second, when the IE offset is fixed, the PCE is primarily governed by the carrier with lower mobility, with minimal dependence on carrier type; and third, with a fixed IE offset and mobility, the PCE is predominantly influenced by the bimolecular recombination rate. When the IE offset was adjusted by varying the optical band gap of the donor, the conclusions remained consistent with the above [see Fig. S11 within the Supplemental Material [41]]. In addition, PCE did not change significantly when the donor band gap was changed, which can be attributed to the fact that the intensity of the sunlight spectrum is highest in the wavelength range of 400–700 nm [see Fig. S13 within the Supplemental Material [42]], and the absorption range of the donor also changes in this range [see Fig. S1(b) within the Supplemental Material [43]]. Ultimately, carrier mobility greater than 1×10^8 m^2/V s, a bimolecular recombination rate lower than 1.3×10^{13} cm^3/s, and an IE offset of 0.3 eV are necessary to achieve a device PCE exceeding 20%.

Finally, we examined the active layer morphology of the bilayer OSCs. Atomic force microscopy and transmission electron microscopy (TEM) were employed to visualize the thin-film morphology of the photoactive layer. As shown in Figs. 4(a)–4(c), the root-mean-square roughness values of the PM6/eC9-0Cl, PM6/eC9-2Cl, and PM6/eC9-4Cl films were 0.87, 0.88, and 0.98 nm, respectively, indicating consistent surface topography across all films. These observations align with the TEM results presented in Figs. 4(d)–4(f). To further quantify the morphological differences, we conducted grazing-incidence wide-angle x-ray scattering measurements [Figs. 4(g)–4(i)] to investigate molecular packing and orientation [see Table S10 within the Supplemental Material [44]]. The (010) π-π stacking peak appeared at q_z values of 1.68, 1.67, and 1.70 Å^1 in the PM6/eC9-0Cl, PM6/eC9-2Cl, and PM6/eC9-4Cl films, corresponding to d-spacing values of 3.74, 3.76, and 3.70 Å, respectively. The q value represents the degree of compactness in π-π stacking, where tighter stacking favors charge transfer. The crystalline coherence length (CCL) values were 20.20, 21.75, and 21.75 Å for the PM6/eC9-0Cl, PM6/eC9-2Cl, and PM6/eC9-4Cl bilayer films, respectively. The larger CCL values suggest enhanced crystallinity and phase separation, which are beneficial for charge transport and extraction.

III. CONCLUSION

In conclusion, we systematically investigated the impact of IE offset on exciton and charge carrier dynamics in bilayer OSCs composed of PM6 paired with eC9-0Cl, eC9-2Cl, and eC9-4Cl. The IE levels of the acceptors were tuned for the chlorination of the acceptor end groups, resulting in IE offset energies of 0.23, 0.30, and 0.47 eV for PM6/eC9-0Cl, PM6/eC9-2Cl, and PM6/eC9-4Cl, respectively. We found that an IE offset of approximately 0.3 eV is needed for effective exciton dissociation, as it reduces bimolecular recombination and enhances both the J_{SC} and FF, thereby improving the PCE of the bilayer OSCs. Furthermore, simulation results indicate that a carrier mobility greater than 1×10^8 m^2/V s and a bimolecular recombination rate lower than 1.3×10^{13} cm^3/s are necessary to achieve a PCE exceeding 20%. Our study underscores the critical role of IE offset energy in exciton dissociation for bilayer OSCs and provides valuable insights for material design.

IV. EXPERIMENTAL METHODS

A. Materials

PM6 was purchased from Dongguan Volt-Amp Optoelectronics Technology Co., Ltd; eC9-0Cl, eC9-2Cl, and eC9-4Cl were purchased from Solarmer, Inc. (Beijing) and Derthon Inc (Shenzhen). Poly(3,4ethylenedioxythiophene) polystyrene sulfonate (PEDOT: PSS) (CLEVIOSTM P VP AI 4083, Heraeus, Germany) was purchased from Xi'an Yuri Solar Co., Ltd. Perylene diimide (PDIN) was purchased from Organtec Ltd.

B. Device fabrication

Bilayer organic solar cells were prepared on glass substrates with tin-doped indium oxide (15 Ω/sq; device area, 0.04 cm^2). Substrates were prewashed with isopropanol to remove organic residues before immersing them in an ultrasonic bath of soap for 15 min. Samples were rinsed in flowing deionized water for 5 min before being sonicated for 15 min each in successive baths of deionized water, acetone, and isopropanol. Next, the samples were dried with pressurized nitrogen before being exposed to a UV-ozone plasma for 15 min. A thin layer of PEDOT:PSS (approximately 20 nm) (Clevios AL4083) was spin-coated

onto the UV-treated substrates, the PEDOT-coated substrates were subsequently annealed on a hot plate at 150 °C for 20 min, and the substrates were then transferred into the glovebox for active-layer deposition.

For the solar cells with a bilayer architecture, PM6 in chloroform solution (8 mg/mL) was spin-coated on the PEDOT: PSS layer to form a front layer, and then a solution of the eC9-XCl (10 mg/mL) in dichloromethane (DCM) were spin onto the donor layer. Then, a methanol solution of PDIN at a concentration of 2.0 mg/ml with acetic acid (0.3 vol %) was spin-coated onto the active layer at 5000 rpm. Next, the substrates were pumped down in a high vacuum at a pressure of 3×10^{-4} Pa, and the Ag layer (100 nm) was thermally evaporated onto the active layer.

C. Photocurrent measurements

The J-V measurement was performed via an XES-50S1 (SANEI Electric Co., Ltd.) solar simulator (AAA grade), whose intensity was calibrated by a certified standard silicon solar cell (SRC-2020, Enlitech) under the illumination of AM1.5G 100 mW cm^{-2}. The AM1.5G light source

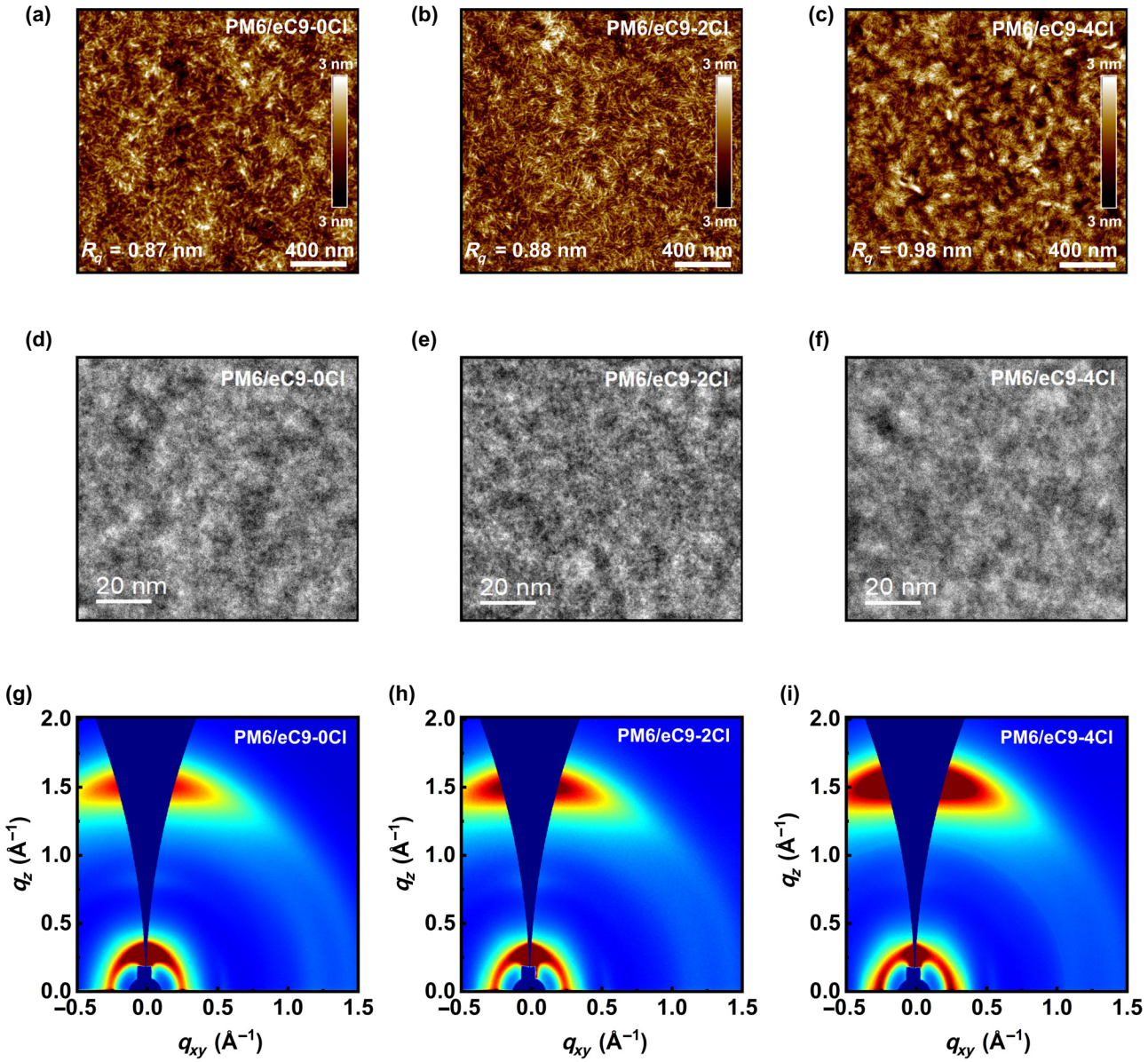

FIG. 4. Atomic force microscopy images of the thin film: (a) PM6/eC9-0Cl, (b) PM6/eC9-2Cl, and (c) PM6/eC9-4Cl. Transmission electron microscopy images of the thin film: (d) PM6/eC9-0Cl, (e) PM6/eC9-2Cl, and (f) PM6/eC9-4Cl. Two-dimensional grazing-incidence wide-angle x-ray scattering patterns of the thin film: (g) PM6/eC9-0Cl, (h) PM6/eC9-2Cl, and (i) PM6/eC9-4Cl.

with a spectral mismatch factor of 1.01 was calibrated by the National Institute of Metrology. The intensity of the AM1.5G spectra was calibrated by a certified standard silicon solar cell (SRC-2020, Enlitech) calibrated by the National Institute of Metrology. The J-V curves of small-area devices were measured in forward scanning mode (from −0.2 to 1.2 V) with a scan step of 0.02 V. The EQE was measured by certified incident photon-to-electron conversion equipment (QE-R) from Enli Technology Co., Lt. The light intensity at each wavelength was calibrated using a standard monocrystalline Si photovoltaic cell. Optoelectronic characterizations were performed with PAIOS (Fluxim, Switzerland).

ACKNOWLEDGMENTS

The authors thank the financial support from the National Natural Science Foundation of China (Grant No. 62275057), and the Guangxi Natural Science Foundation (Grants No. 2023GXNSFFA026004 and No. 2022GXNSFDA035066). Portions of this research were carried out at the 3C SAXS-I and 9A U-SAXS beamlines of the Pohang Accelerator Laboratory (PLS-II), Republic of Korea. This work is also supported by the Guangxi Talent Program ("Highland of Innovation Talents").

The authors declare no competing interests.

DATA AVAILABILITY

The data that support the findings of this article are openly available.

[1] D. Meng, R. Zheng, Y. Zhao, E. Zhang, L. Dou, and Y. Yang, Near-infrared materials: The turning point of organic photovoltaics, Adv. Mater. **34**, 2107330 (2022).

[2] J. Wang, Z. Zheng, P. Bi, Z. Chen, Y. Wang, X. Liu, S. Zhang, X. Hao, M. Zhang, Y. Li, and J. Hou, Tandem organic solar cells with 20.6% efficiency enabled by reduced voltage losses, Natl. Sci. Rev. **10**, nwad085 (2023).

[3] G. Zhang, F. Lin, F. Qi, T. Heumüller, A. Distler, H. Egelhaaf, N. Li, P. Chow, C. Brabec, A. Jen, and H. Yip, Renewed prospects for organic photovoltaics, Chem. Rev. **122**, 14180 (2022).

[4] F. Zhao, H. Zhang, R. Zhang, J. Yuan, D. He, Y. Zou, and F. Gao, Emerging approaches in enhancing the efficiency and stability in non-fullerene organic solar cells, Adv. Energy Mater. **10**, 2002746 (2020).

[5] L. Dou, J. You, Z. Hong, Z. Xu, G. Li, R. A. Street, and Y. Yang, 25th anniversary article: A decade of organic/polymeric photovoltaic research, Adv. Mater. **25**, 6642 (2013).

[6] Z. Zhao, S. Chung, Y. Kim, M. Jeong, X. Li, J. Zhao, C. Zhu, S. Karuthedath, Y. Zhong, K. Cho, and Z. Kan, Room-temperature-modulated polymorphism of non-fullerene acceptors enables efficient bilayer organic solar cells, Energy Environ. Sci. **17**, 5666 (2024).

[7] Y. Jiang, S. Sun, R. Xu, F. Liu, X. Miao, G. Ran, K. Liu, Y. Yi, W. Zhang, and X. Zhu, Non-fullerene acceptor with asymmetric structure and phenyl-substituted alkyl side chain for 20.2% efficiency organic solar cells, Nat. Energy **9**, 975 (2024).

[8] C. Li, G. Yao, X. Gu, J. Lv, Y. Hou, Q. Lin, N. Yu, M. Abbasi, X. Zhang, J. Zhang, Z. Tang, Q. Peng, C. Zhang, Y. Cai, and H. Huang, Highly efficient organic solar cells enabled by suppressing triplet exciton formation and non-radiative recombination, Nat. Commun. **15**, 8872 (2024).

[9] S. Karuthedath, J. Gorenflot, Y. Firdaus, N. Chaturvedi, C. Castro, G. Harrison, J. Khan, A. Markina, A. Balawi, T. Peña, *et al.*, Intrinsic efficiency limits in low-bandgap non-fullerene acceptor organic solar cells, Nat. Mater. **20**, 3 (2021).

[10] D. C. Coffey, B. W. Larson, A. W. Hains, J. B. Whitaker, N. Kopidakis, O. V. Boltalina, S. H. Strauss, and G. Rumbles, An optimal driving force for converting excitons into free carriers in excitonic solar cells, J. Phys. Chem. C **116**, 8916 (2012).

[11] S. Karuthedath, J. Gorenflot, A. Melianas, Z. Kan, M. Kemerink, and F. Laquai, Buildup of triplet-state population in operating TQ1:PC71BM devices does not limit their performance, J. Phys. Chem. Lett. **11**, 2838 (2020).

[12] K. H. Hendriks, A. S. G. Wijpkema, J. J. van Franeker, M. M. Wienk, and R. A. J. Janssen, Dichotomous role of exciting the donor or the acceptor on charge generation in organic solar cells, J. Am. Chem. Soc. **138**, 10026 (2016).

[13] S. Li, L. Zhan, C. Sun, H. Zhu, G. Zhou, W. Yang, M. Shi, C. Li, J. Hou, Y. Li, and H. Chen, Highly efficient fullerene-free organic solar cells operate at near zero highest occupied molecular orbital offsets, J. Am. Chem. Soc. **141**, 3073 (2019).

[14] J. S. Müller, M. Comí, F. Eisner, M. Azzouzi, D. Herrera Ruiz, J. Yan, S. S. Attar, M. Al-Hashimi, and J. Nelson, Charge-transfer state dissociation efficiency can limit free charge generation in low-offset organic solar cells, ACS Energy Lett. **8**, 3387 (2023).

[15] Y. Tamai, R. Shirouchi, T. Saito, K. Kohzuki, and S. Natsuda, Role of the energy offset in the charge photogeneration and voltage loss of nonfullerene acceptor-based organic solar cells, J. Mater. Chem. A **11**, 17581 (2023).

[16] G. Wen, R. Hu, J. Feng, J. Peng, Z. Chen, C. Zhang, N. Zhao, X. Zou, Z. Chen, C. Liu, and W. Zhang, Energy level offsets determine the interplay between charge and energy transfer in all-small-molecule organic solar cells, Chem. Eng. J. **475**, 145939 (2023).

[17] S. Sweetnam, K. R. Graham, G. O. Ngongang Ndjawa, T. Heumüller, J. A. Bartelt, T. M. Burke, W. Li, W. You, A. Amassian, and M. D. McGehee, Characterization of the polymer energy landscape in polymer:fullerene bulk heterojunctions with pure and mixed phases, J. Am. Chem. Soc. **136**, 14078 (2014).

[18] N. Tokmoldin, B. Sun, F. Moruzzi, A. Patterson, O. Alqahtani, R. Wang, B. Collins, I. McCulloch, L. Lüer, C. Brabec, D. Neher, and S. Shoaee, Elucidating how low energy offset matters to performance of nonfullerene acceptor-based solar cells, ACS Energy Lett. **8**, 2552 (2023).

[19] J. Feng, G. Wen, R. Hu, J. Peng, H. Lu, N. Zhao, X. Zou, and W. Zhang, The role of energy offsets on charge photogeneration dynamics in Y-series molecules-based polymer solar cells, Sol. RRL **7**, 2300372 (2023).
[20] See Supplemental Material at http://link.aps.org/supplemental/10.1103/PhysRevApplied.23.034006 for the non-normalized UV-vis spectra.
[21] See Supplemental Material at http://link.aps.org/supplemental/10.1103/PhysRevApplied.23.034006 for the detailed information on the analysis of IE and EA values.
[22] See Supplemental Material at http://link.aps.org/supplemental/10.1103/PhysRevApplied.23.034006 for the absorption spectra of donor before and after solvent washing.
[23] See Supplemental Material at http://link.aps.org/supplemental/10.1103/PhysRevApplied.23.034006 for the dark current of the device.
[24] X. Song, K. Zhang, R. Guo, K. Sun, Z. Zhou, S. Huang, L. Huber, M. Reus, J. Zhou, M. Schwartzkopf, *et al.*, Process-aid solid engineering triggers delicately modulation of Y-series non-fullerene acceptor for efficient organic solar cells, Adv. Mater. **34**, 2200907 (2022).
[25] See Supplemental Material at http://link.aps.org/supplemental/10.1103/PhysRevApplied.23.034006 for the details of the PLQE of the device.
[26] D. Bozyigit, M. Jakob, O. Yarema, and V. Wood, Deep level transient spectroscopy (DLTS) on colloidal-synthesized nanocrystal solids, ACS Appl. Mater. Interfaces **5**, 2915 (2013).
[27] R. Li, B. Li, X. Fang, D. Wang, Y. Shi, X. Liu, R. Chen, and Z. Wei, Self-structural healing of encapsulated perovskite microcrystals for improved optical and thermal stability, Adv. Mater. **33**, 2100466 (2021).
[28] Y. Zhang, G. Cai, Y. Li, Z. Zhang, T. Li, X. Zuo, X. Lu, and Y. Lin, An electron acceptor analogue for lowering trap density in organic solar cells, Adv. Mater. **33**, 2008134 (2021).
[29] B. Feng, J. Zhao, S. Chung, K. Cho, S. Lu, W. Xu, and Z. Kan, Regulating the donor–acceptor interfaces to reduce trap density for efficient indoor organic solar cells, Sol. RRL **7**, 2200989 (2023).
[30] J. Zhou, D. He, Y. Li, F. Huang, J. Zhang, C. Zhang, Y. Yuan, Y. Lin, C. Wang, and F. Zhao, Reducing trap density in organic solar cells via extending the fused ring donor unit of an A–D–A-type nonfullerene acceptor for over 17% efficiency, Adv. Mater. **35**, 2207336 (2023).
[31] Z. Zhao, J. Zhao, S. Chung, K. Cho, W. Xu, and Z. Kan, Suppressing bimolecular charge recombination and energetic disorder with planar heterojunction active layer enables 18.1% efficiency binary organic solar cells, ACS Mater. Lett. **5**, 1718 (2023).
[32] See Supplemental Material at http://link.aps.org/supplemental/10.1103/PhysRevApplied.23.034006 for the details of the trap state density of the device.
[33] X. Meng, C. H. Y. Ho, S. Xiao, Y. Bai, T. Zhang, C. Hu, H. Lin, Y. Yang, S. K. So, and S. Yang, Molecular design enabled reduction of interface trap density affords highly efficient and stable perovskite solar cells with over 83% fill factor, Nano Energy **52**, 300 (2018).
[34] A. Pivrikas, G. Juška, A. Mozer, M. Scharber, K. Arlauskas, N. Sariciftci, H. Stubb, and R. Österbacka, Bimolecular recombination coefficient as a sensitive testing parameter for low-mobility solar-cell materials, Phys. Rev. Lett. **94**, 176806 (2005).
[35] See Supplemental Material at http://link.aps.org/supplemental/10.1103/PhysRevApplied.23.034006 for the details of the bimolecular recombination rate of the device.
[36] See Supplemental Material at http://link.aps.org/supplemental/10.1103/PhysRevApplied.23.034006 for the dependence of IE offset on transient photocurrent, transient photovoltage, bimolecular recombination, and trap state density.
[37] See Supplemental Material at http://link.aps.org/supplemental/10.1103/PhysRevApplied.23.034006 for the device structure under simulated conditions.
[38] See Supplemental Material at http://link.aps.org/supplemental/10.1103/PhysRevApplied.23.034006 for the evolution of the figures of PCE of OPV device as a function of minority carriers to majority carriers in donor and acceptor.
[39] M. Pu, C. Cao, H. Chen, Y. Zhu, P. Tan, X. Lai, and F. He, Optimized bicontinuous interpenetrating network morphology formed by gradual chlorination to boost photovoltaic performance, Chem. Eng. J. **437**, 135198 (2022).
[40] D. Li, H. Zhang, X. Cui, Y. Chen, N. Wei, G. Ran, H. Lu, S. Chen, W. Zhang, C. Li, *et al.*, Halogenated nonfused ring electron acceptor for organic solar cells with a record efficiency of over 17%, Adv. Mater. **36**, 2310362 (2024).
[41] See Supplemental Material at http://link.aps.org/supplemental/10.1103/PhysRevApplied.23.034006 for the effect of carrier mobility on PCE and bimolecular recombination rate at different IE migrations.
[42] See Supplemental Material at http://link.aps.org/supplemental/10.1103/PhysRevApplied.23.034006 for the sunlight spectrum.
[43] See Supplemental Material at http://link.aps.org/supplemental/10.1103/PhysRevApplied.23.034006 for the absorption spectra of donor with different optical band gaps.
[44] See Supplemental Material at http://link.aps.org/supplemental/10.1103/PhysRevApplied.23.034006 for the detailed parameters of grazing-incidence wide-angle x-ray scattering with the device.